AIAA JOURNAL
Vol. 33, No. 2, February 1995

Quantitative Comparison Between Interferometric Measurements and Euler Computations for Supersonic Cone Flows

T. A. W. M. Lanen,* E. M. Houtman,† and P. G. Bakker‡
Delft University of Technology, Delft, The Netherlands

Dual-reference-beam, plane-wave digital holographic interferometry has been applied to obtain quantitative interferometric data in the three-dimensional supersonic flow over circular cones. The interferometric data are compared quantitatively on a two-dimensional grid with the postprocessed results of an Euler code that simulates three-dimensional inviscid compressible flows. The comparison involves two different combinations of cone angle and angle of incidence. The maximum deviations between the interferometric data and the numerical data are found to lie in the error interval [−2.0%, +2.0%].

I. Introduction

TO validate numerical codes for the simulation of three-dimensional compressible flows, extensive experimental flowfield data are required. The nonintrusiveness and the high resolution of the data provided by a single measurement (512 × 512 data points) make digital holographic interferometry (DHI) in some respects a good alternative for conventional measuring techniques like pressure probe measurements. DHI is the optical measuring technique that combines holographic interferometry to visualize the flowfield in an interferogram, phase stepping of the interferogram and digital image processing to compute the phase map from the digitized interferograms. The phase map reflects the deformation of the wave fronts of a laser light beam that has passed through the flowfield inside a test section. The phase is proportional to the mean density over the width of the test section along the direction of light propagation. At the same time, this explains the inherent disadvantage of DHI. In three-dimensional flows it provides only quantitative information about the average density along light rays through the flowfield.

In this paper the experimental data provided by DHI will be compared with the numerical data obtained by a computer code for inviscid compressible flow (three-dimensional Euler code). The supersonic flow around circular cones will serve as the test flowfield in the comparison. Several good reasons exist for choosing this flowfield as the test flowfield. First, if the bow shock is attached, it represents a relatively simple flowfield because of its conical symmetry. In this case no dominant viscous interaction effects are present and the assumption of an inviscid fluid holds. Furthermore, extensive results of inviscid flow computations are available for several Mach numbers M_∞, angles of incidence α, and cone half-angles θ_c.[1-3] Finally, the applicability of holographic interferometry in the investigation of the supersonic flow around circular cones has been successfully demonstrated before.[4,5]

II. Experimental Setup

The experiments were carried out in a blowdown wind tunnel equipped with a symmetrical supersonic nozzle, generating a nominal Mach 3 uniform supersonic flow around the circular cone in the test section area. Figure 1 shows the holographic interferometer used in the experiments. The interferometer uses a pulsed ruby laser ($\lambda = 693.4$ nm) to expose a holographic plate and a CW HeNe laser ($\lambda = 632.8$ nm) to reconstruct the hologram. For a detailed description of this setup the reader is referred to earlier literature.[6] In Fig. 1 also the test section of the wind tunnel (with cross-sectional dimensions of 150 × 150 mm^2) has been indicated. The main flow direction in the test section is oriented normal to the plane of drawing. The test section is traversed by parallel laser light.

In supersonic flow the presence of the cone model will only affect the flow quantities in the area bounded by the attached bow shock wave and the cone surface. The axial symmetry of the flow allows the nondimensional density ρ/ρ_∞ to be presented by a single curve as a function of the nondimensional distance to the cone surface ξ, which is defined as

$$\xi = \frac{\tan\theta - \tan\theta_c}{\tan\theta_s - \tan\theta_c} \tag{1}$$

Figure 2 shows the radial density distribution around a 15-deg half-angle cone at 0-deg incidence in Mach 3 supersonic flow.[2] In this definition all angles are measured relative to the axis of the cone, and θ_s indicates the attached bow shock wave.

The limited extent of the flow region influenced by the presence of the cone allows us to reduce the disturbing effects on the interferometric measurements due to sidewall boundary layers. This is achieved by a streamwise translation of the cone model between the two exposures of the holographic plate in one wind-tunnel run. Figure 3 shows in side view (i.e., through one of the test section windows) the position of the cone model during the first exposure, taken at $T = T_1$ and its position at $T = T_2$ when the second exposure is taken. In this figure the area of the flowfield (±75 × 75 mm^2) that will be imaged on the CCD camera during reconstruction of the hologram has also been indicated. Because the scene beam traverses the sidewall boundary layers on the test section windows for both holographic exposures, their effect will be canceled in the interferogram. Obviously, total cancellation will only be achieved if the sidewall boundary layers reproduce exactly between the two moments of exposure. This will more likely occur for the shorter time intervals $\Delta t = T_2 - T_1$. In the cone measurements to be presented the time interval is about $\Delta t \approx 10$ s. Total cancellation may not be expected in the present measurements for yet another reason. Because the bow shock wave from the cone impinges on the sidewall boundary layers at different locations for the two exposures due to the translation of the cone model, the bow shock wave/sidewall boundary-layer interaction will affect the upstream boundary layers on the test section windows differently through their subsonic sublayers.

As an additional advantage of the aforementioned strategy, it must be remarked that steady deviations from uniform supersonic flow conditions, which are known to exist in the interior flow of the wind tunnel due to nozzle surface imperfections and sidewall irregularities, will be canceled partly in the interferogram.

Presented as Paper 92-2691 at the AIAA 10th Applied Aerodynamics Conference, Palo Alto, CA, June 22–24, 1992; received April 18, 1994; revision received Aug. 3, 1994; accepted for publication Aug. 20, 1994.

*Research Scientist, Department of Aerospace Engineering, P.O. Box 5058, NL-2600 GB.

†Assistant Professor, Department of Aerospace Engineering, P.O. Box 5058, NL-2600 GB.

‡Professor, Department of Aerospace Engineering, P.O. Box 5058, NL-2600 GB.

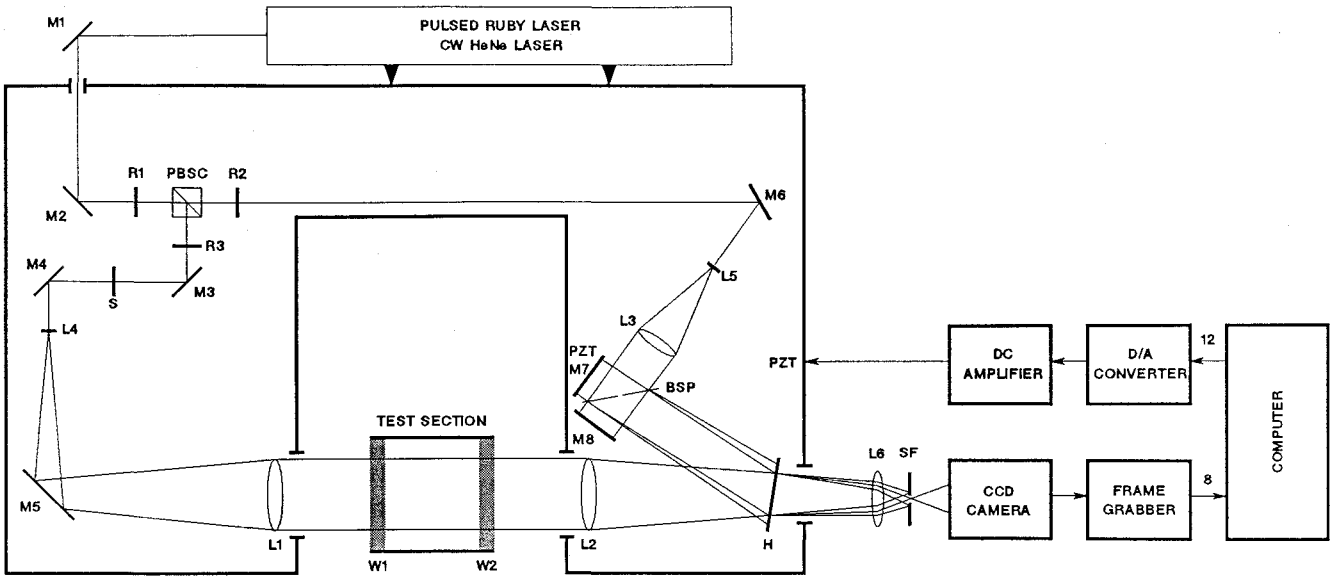

Fig. 1 Dual-reference-beam, plane-wave holographic interferometer connected to computer system.

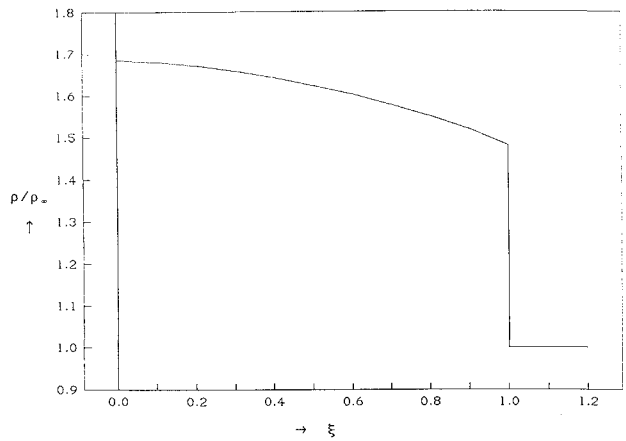

Fig. 2 Typical nondimensional density distribution ρ/ρ_∞ around a cone in uniform supersonic flow vs dimensionless distance to cone surface $\xi(\theta_c = 15\,\text{deg}, \alpha = 0\,\text{deg}, \text{and } M_\infty = 3)^2$.

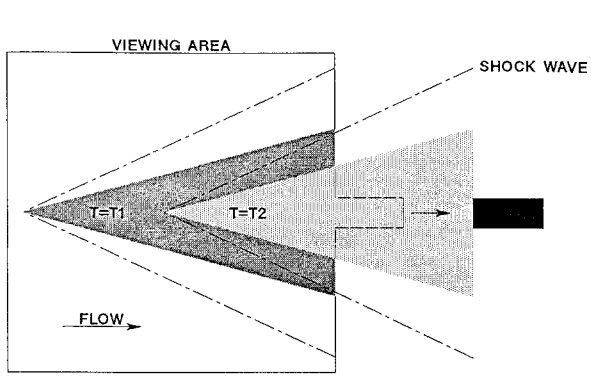

Fig. 3 Streamwise translation of cone model between successive exposures of holographic plate.

The just-described procedure has been followed to obtain quantitative interferometric data by DHI for two combinations (θ_c, α) of cone half-angle and nominal angle of incidence: (15 deg, 0 deg) and (10 deg, 10 deg). The results of the measurements will be described later. In addition to the interferometric measurements, the stagnation pressure, the temperature in the settling chamber, and the pitot pressure in the test section have been measured. From these quantities the Mach number in the oncoming supersonic stream M_∞ (= 2.95) and the freestream density ρ_∞ (= 0.70 kg/m^3) are determined.

III. Experimental and Numerical Results

A. Circular Cone: $\theta_c = 15$ Deg, $\alpha = 0.45$ Deg

Figure 4 shows the phase map modulo 2π rad obtained with the setup of Fig. 1 of the flow around the cone. The region shown by Fig. 4 corresponds to an area of 75.4 × 75.4 mm^2 in the test section. Besides a slight asymmetry between the fringes at the upper side and at the lower side of the cone due to a small positive angle of incidence (measured as $\alpha = 0.45$ deg), two phenomena attract the attention in this figure.

1. Reproducibility of Oncoming Supersonic Flow

From Fig. 4 it follows directly that the oncoming supersonic stream does not reproduce exactly over the time interval Δt between the two exposures of the holographic plate and that the differences manifest themselves in streamwise direction. This may be attributed to changes in the sidewall boundary layers on the test section windows due to the translation of the cone (see earlier remarks) or due to unsteadiness of the flow. In the phase map of Fig. 4 the peak-to-peak phase value in the oncoming flow due to the limited reproducibility is found to be equal to 0.47λ. In terms of the average density over the width of the test section (L = 150 mm) where a phase difference of 2π rad equals a density difference of 0.021 kg/m^3, this corresponds to a peak-to-peak deviation of the density from the freestream density ρ_∞ of less than 1.4%. Though this percentage seems quite reasonable, one should realize that it is related to the average density over the width of the test section and hence that local variations in the three-dimensional density distribution in the supersonic flow between the two moments of exposure may be larger.

2. Sampling Considerations

Furthermore, the phase map of Fig. 4 shows strong gradients at the location of the shock wave that are visible as regions of high-frequency fringe spacing. Therefore, one should be careful when the 2π discontinuities are removed from the phase map by phase unwrapping.[6] A necessary condition for correct execution of this image-processing step is that the sampling criterion (i.e., the minimum sampling frequency must be larger than 2 pixels/fringe) is satisfied at all pixels of the phase map. Regions of the phase map where the sampling criterion is violated must be circumvented. It can be shown that the gradient in the phase map shows a maximum magnitude at the projected shock wave and that the gradient is oriented here along the direction normal to the shock wave. This can also be concluded from Fig. 4 because the fringes close to the shock wave are oriented parallel to it. The two parameters that determine the magnitude of the phase gradient at the shock wave are the local radius of curvature of the shock wave and the density jump across

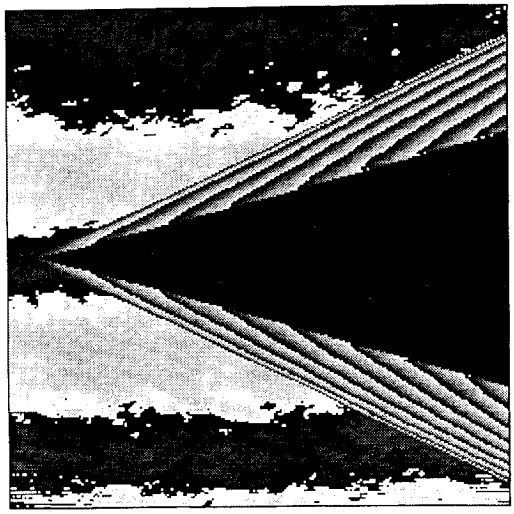

Fig. 4 Phase map modulo 2π rad of the flow around the cone (size 75.4 × 75.4 mm^2).

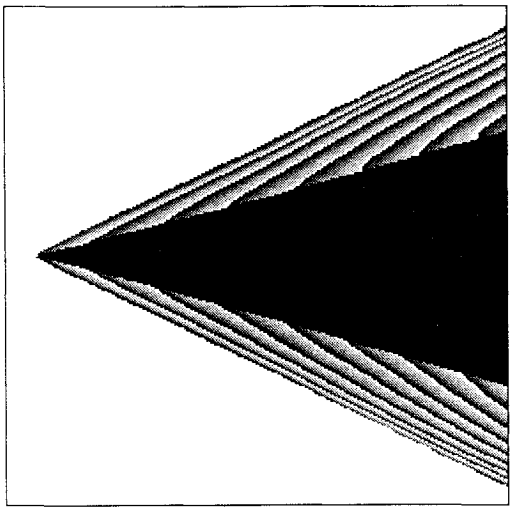

Fig. 5 Binary mask indicating location of circular cone and high-frequency fringe-spacing pixels.

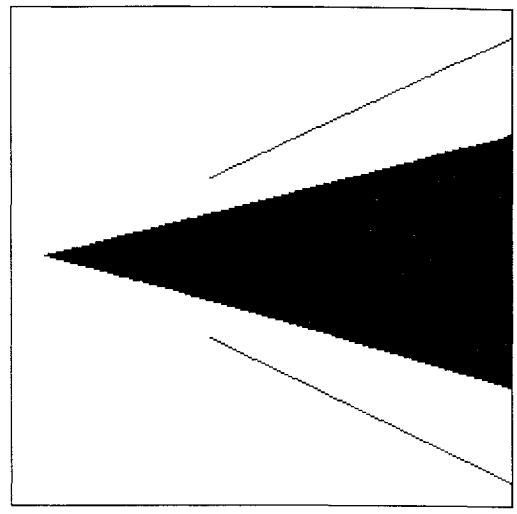

Fig. 6 Measured phase map after (7, 7) phase fitting (interval range λ).

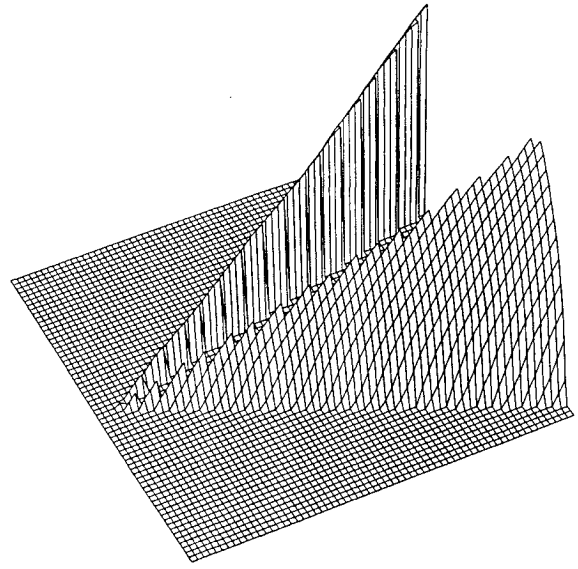

Fig. 7 Quasi-three-dimensional plot of measured phase map (64 × 64 grid points).

the shock wave. The larger the radius of curvature and the larger the density jump, the larger the magnitude of the phase gradient will be. Therefore, the phase gradient will be stronger for pixels on the projected shock wave further away from the apex of the cone. Figure 5 shows the binary mask that was determined to mark the location of the circular cone and the pixels on the projected shock wave in Fig. 4 not satisfying the sampling criterion.

3. Unwrapped Phase Map

Figure 6 shows the unwrapped phase map after a bilinear interpolation over a window of size (7, 7). Figure 7 shows the phase map as a quasi-three-dimensional plot. The interpolation served to restore the phase at the location of the shock wave. A relatively small filter size was chosen to avoid blurring of the shock wave. No attempts have been made to compute the radial density distribution in the flow around the cone from Figs. 6 and 7 by application of the inverse Abel transform.[7] Since the angle of incidence of the cone deviates considerably from zero ($\alpha = 0.45$ deg), the condition of a completely axisymmetric flowfield is not fulfilled. Comparison with the numerically computed three-dimensional density distribution around the cone can therefore not be carried out on the interface of the density but necessarily has to be carried out on the interface of the phase (which is proportional to the average density over the width of the test section). This is a common procedure since experimentally observed flowfields generally do not possess axial symmetry and the comparison with interferometric data in these cases has to be carried out on the interface of the phase anyway. So to compare with experimental data, the computed three-dimensional density distribution must be postprocessed to a two-dimensional phase map by integration of the density along light rays. Furthermore, the comparison will be less detailed since positive and negative errors will be partly canceled both in the optical integration and in the numerical integration.

4. Numerical Computation of Phase Map

A numerical computation of the density distribution around the cone has been carried out using a three-dimensional Euler code. This code is based on a finite volume discretization of the steady three-dimensional Euler equations and uses an upwind spatial differencing technique (van Leer's flux-vector splitting). This code yields the three-dimensional density distribution, $\rho_{3D}(x, y, z)$, around the cone on a regular but not equidistant three-dimensional grid, consisting of $48 \times 48 \times 48$ finite volumes. The computations were performed for the same freestream conditions as in the experiments. The angle of incidence α of the cone was measured in the wind tunnel as 0.45 deg. The phase map was computed from the three-dimensional density distribution by evaluation of the density along straight ray paths. In this way a transition is made from the three-dimensional grid on which the computed density is given to the equidistant two-dimensional grid of pixels. The postprocessing step of the numerical solution involves a computationally expensive interpolation procedure on the three-dimensional numerical data to produce the density on a large amount of points on the rays of light, followed by an

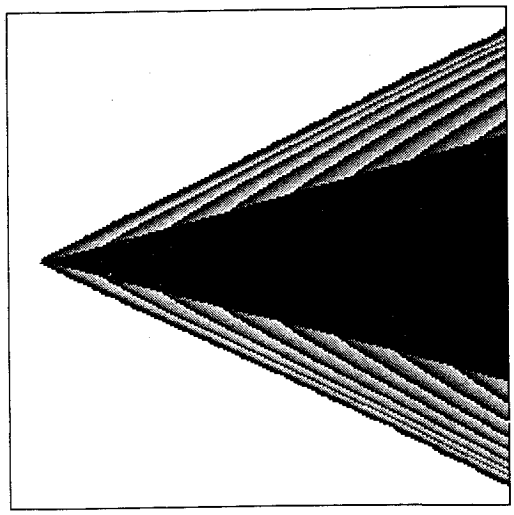

Fig. 8 Computed phase map of supersonic flow around a circular cone using a three-dimensional Euler code (interval range λ).

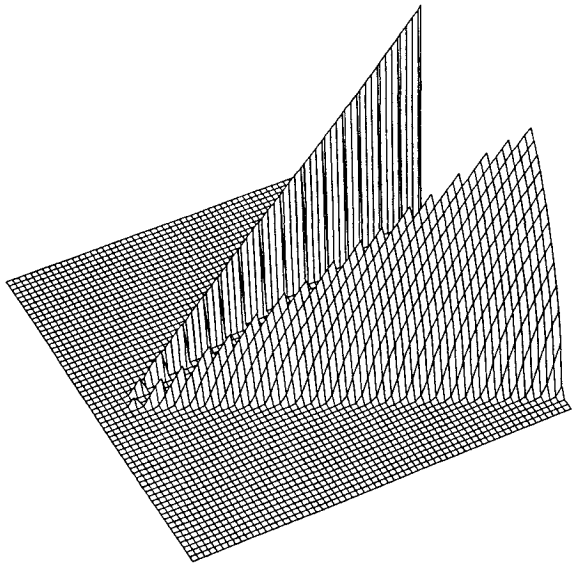

Fig. 9 Quasi-three-dimensional plot of computed phase map (64 × 64 grid points).

integration of the density along the light rays using the trapezoidal rule. To enable a pixelwise comparison with the interferometric data, the orientation of the cone model with respect to the detector grid has to be considered during the integration. The orientation of the cone is determined from the binary mask of Fig. 5. Furthermore, scaling of the computed phase map is done by accounting for the size of the area in the wind tunnel that is imaged on the CCD camera in the interferometric measurements. This size is determined by reconstruction of a third hologram on which a transparent ruler, placed in the plane of the wind tunnel containing the axis of the cone, has been recorded. Together with the aforementioned values of the Gladstone-Dale constant, the wavelength of the ruby laser, and the freestream density, the phase map shown in Figs. 8 and 9 has been computed. Though being continuous, just as the measured phase map of Fig. 6 it has also been depicted on the λ-interval range in Fig. 8 to allow a direct comparison.

5. Comparison of Experimental and Numerical Results

From Figs. 6 and 8 it follows that the computational results and the experimental data qualitatively show very good agreement. The first impression is that the two phase maps show no differences at all. However, a closer look reveals a stronger bending of the interference fringes towards the surface of the cone in the measured phase map as compared with the computed phase map. This is caused by the presence of a boundary layer at the surface of the cone in which the density decreases when approaching the surface. However, this

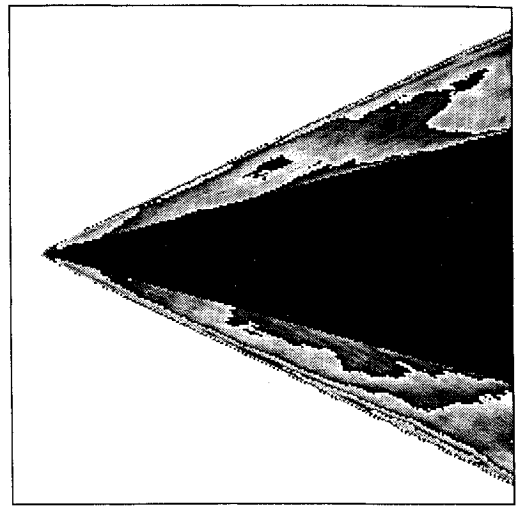

Fig. 10 Phase map obtained by subtraction of the measured phase map of Fig. 6 from the computed phase map of Fig. 8 [interval range (1/5)λ].

boundary layer is not modeled by the Euler equations for inviscid flow, and hence in the numerical data the density increases monotonically towards the surface of the cone (see also Fig. 2). Therefore, the unwrapped phase map (which is proportional to the average density over the width of the test section) shows phase values near the surface of the cone that are smaller in the measurements than those predicted by the computations, explaining the extra bending of the interference fringes in Fig. 6.

These and other differences are more clearly demonstrated by a quantitative comparison of Figs. 6 and 8. The total number of (interference) fringes at the upper side and at the lower side of the cone found in the computation and in the experiment correspond remarkably well. The absolute difference between the computed and the measured total number of interference fringes at the upper side and at the lower side of the cone is found to be less than 0.01λ. Hence, the asymmetry of the flowfield due to the small positive angle of incidence is modeled quite well. Because the orientation of the cone in the computed phase map was chosen identical to its orientation in the measured phase map, the phase values of the two phase maps can be compared at corresponding pixels. Figure 10 shows the phase map that results by a pixelwise subtraction of the phase map of Fig. 6 from the phase map of Fig. 8. The interval range in this figure equals $(1/5)\lambda$. On both sides of the cone, positive phase differences are found in the region bounded by the surface of the cone and the first black-to-white transition next to the cone. Beyond this black-to-white transition mainly negative phase differences are found. The range of the phase difference in the region enclosed by the projected shock wave and the surface of the cone is approximately equal to $(3/5)\lambda$ on either side of the cone (see Fig. 10). The maximum and minimum phase differences are equal to $+0.14\lambda$ (in the boundary layer at the lower side of the cone) and -0.69λ (at the lower shock wave), respectively. The corresponding error in the density will be computed analogously to the definition followed earlier to quantify the limited reproducibility of the oncoming supersonic stream. The phase difference between the measured phase map and the computed phase map (Fig. 10) corresponds to a deviation in average density over the test section width. The error ϵ in the density will be defined relative to the measured average density over the test section width $\bar{\rho}_{\text{meas}}(x, y)$ (being the sum of the freestream density and the surplus density obtained from the measured phase map) as

$$\epsilon(x, y) = \frac{\bar{\rho}_{\text{comp}}(x, y) - \bar{\rho}_{\text{meas}}(x, y)}{\bar{\rho}_{\text{meas}}(x, y)} \tag{2}$$

In this definition maximum and minimum error percentages of $+0.4\%$ and -2.0%, respectively, are found. These percentages are of the same order of magnitude as the deviation in the density due to the limited reproducibility of the oncoming supersonic stream between the two exposures of the holographic plate. Hence, besides a good qualitative agreement there also exists a good quantitative

agreement between the experimental data obtained by the interferometric measurements and the numerical data provided by the Euler computations. Again because of the integration along light rays, it must be remarked that the local deviations between the experimental three-dimensional density distribution and the computed three-dimensional density distribution may be larger.

B. Circular Cone: $\theta_c = 10$ Deg, $\alpha = 9.83$ Deg

1. Inviscid Flow Around a Cone at Incidence

A similar experiment as just described has been carried out for a cone at incidence, generating a largely nonaxisymmetric flow. The cone half-angle in the present experiment is $\theta_c = 10$ deg. The cone is positioned in the Mach 2.95 supersonic flow in the test section of the wind tunnel at the angle of incidence measured as $\alpha = 9.83$ deg. The expected asymmetry of the flow is illustrated by the numerical results for inviscid flow in Figs. 11 and 12.[2] Figure 11 shows the dimensionless density distribution ρ/ρ_∞ around the cone in a plane normal to the axis of the cone for several circumferential angles Φ. The angle $\Phi = 0$ deg corresponds with the windward plane of symmetry, and $\Phi = 180$ deg corresponds with the leeward plane of symmetry. At the leeward side of the cone the density almost equals the freestream density, and the density at the shock wave only slightly exceeds the freestream density (Fig. 11). A different situation exists at the windward side of the cone. Here the density everywhere is considerably larger than the freestream density, and the location of the shock wave is marked by a strong density jump (Fig. 11). Furthermore, it follows from Fig. 11 that, contrary to the axisymmetric flow of Fig. 2, the density gradually decreases close to the surface of the cone for almost all circumferential angles. Besides the asymmetric density distribution, also a geometrical asymmetry exists because the angle between the shock wave and the axis of the cone θ_s varies with the circumferential angle. This is illustrated by Fig. 12, which shows that the larger values of θ_s are found at the leeward side of the cone.

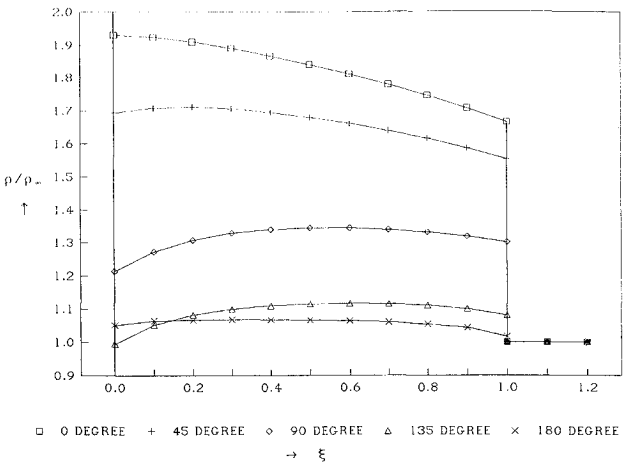

Fig. 11 Typical nondimensional density distribution ρ/ρ_∞ around a cone at incidence in supersonic flow vs dimensionless distance to cone surface ξ for several circumferential angles ($\theta_c = 10$ deg, $\alpha = 10$ deg, and $M_\infty = 3$)[2].

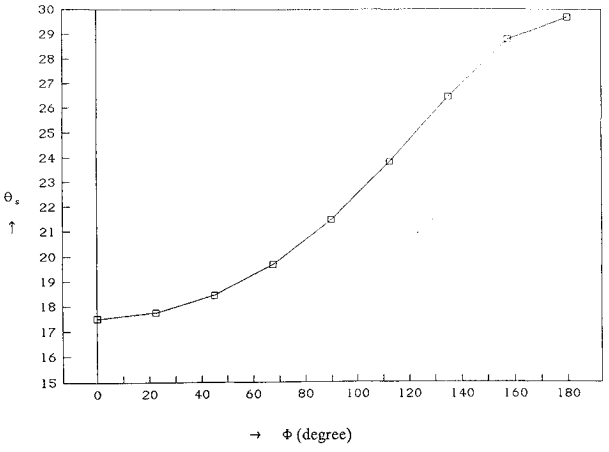

Fig. 12 Variation of angle between shock wave and cone axis θ_s with the circumferential angle Φ($\theta_c = 10$ deg, $\alpha = 10$ deg, and $M_\infty = 3$).[2]

2. Measured and Computed Phase Map

The asymmetry of the flow around the cone is visible in the measured phase map of Fig. 13 by a substantial difference in the total number of interference fringes found at windward side (6.93 fringes) and at the leeward side (1.54 fringes). The asymmetry is also clearly demonstrated by Fig. 14, which depicts the measured phase map as a quasi-three-dimensional plot. Because of the weak shock wave and the relatively low densities at the leeward side, the transition from the undisturbed flow to the disturbed flow at this side of the cone is not marked by a sudden increase of the phase. Therefore, phase unwrapping of the phase map could be carried out across the leeward shock wave without inducing errors. However, just as in the procedure followed in the near axisymmetric flow case (Fig. 5), the location of the windward shock wave had to be marked in a binary mask and had to be circumvented during phase unwrapping.

At the leeward side of the cone the measured phase map shows a wavy character. This may be caused by local small deviations from a uniform supersonic flow that in particular are visible in regions of the phase map where only small phase gradients exist as is the case at the leeward side. The peak-to-peak phase deviation in the oncoming supersonic flow amounts to 0.42λ, being 1.2% of the freestream density. The apparent bending of the interference fringe close to the surface of the cone at the leeward side (Fig. 13) reveals the presence

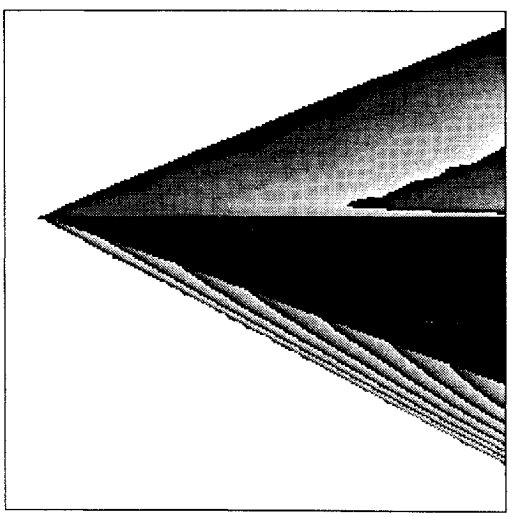

Fig. 13 Measured phase map after (7, 7) phase fitting (size 75.3 × 75.3 mm^2 and interval range λ).

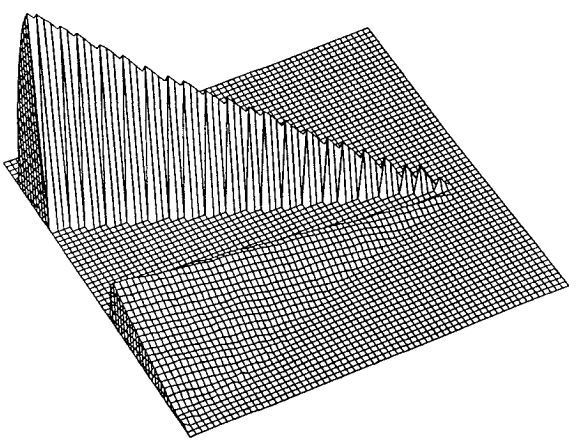

Fig. 14 Quasi-three-dimensional plot of measured phase map (64 × 64 grid points).

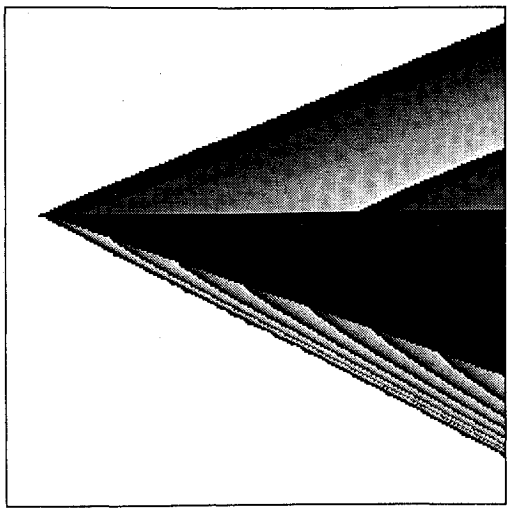

Fig. 15 Computed phase map of supersonic flow about a circular cone using a three-dimensional Euler code (interval range λ).

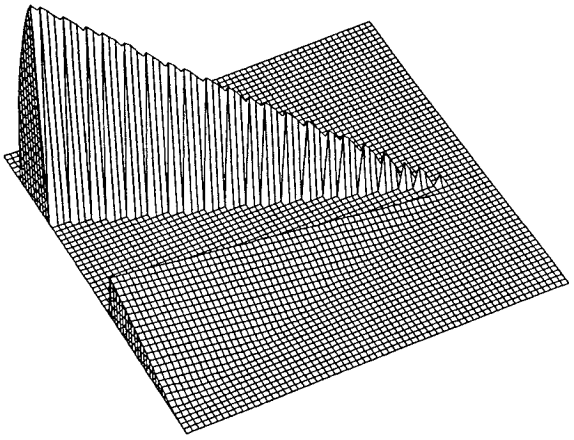

Fig. 16 Quasi-three-dimensional plot of computed phase map (64×64 grid points).

of a boundary layer. Despite the fact that in inviscid flow the density decreases near the surface of the cone at the leeward side (Fig. 11), this sharp bending of the interference fringes is not seen in the phase map based on the three-dimensional Euler computations for inviscid flow (Figs. 15 and 16). Hence, the strong bending in Fig. 13 must unmistakably be attributed to the presence of the boundary layer, which is known to be rather thick at the leeward side of the cone.

3. Comparison of Experimental and Numerical Results

The total number of interference fringes in the computed phase map at the windward side and at the leeward side of the cone is equal to 1.46 and 7.02, respectively. At the leeward side the total number of computed interference fringes is smaller than the number of measured fringes, whereas at the windward side the opposite effect occurs. A similar trend is found in the phase map of Fig. 17, which is obtained by a pixelwise subtraction of the measured phase map of Fig. 13 from the computed phase map of Fig. 15. Positive phase differences are mainly found at the windward side, and negative phase differences are mostly found at the leeward side. An explanation for this tendency is that the real angle of incidence during the interferometric measurements may have been slightly smaller than the measured angle of incidence used as input to the Euler computation. However, another explanation is that the difference in displacement thickness of the windward boundary layer and the leeward boundary layer causes a reduction in the effective angle of incidence. In combination with the known sensitivity of the phase map to the angle of incidence (see Figs. 6 and 8), this may explain the observed trend in the phase map of Fig. 17. The phase map also shows the presence of the boundary layer at the leeward side of the cone, by a region close to the surface of the cone with positive phase differences. The

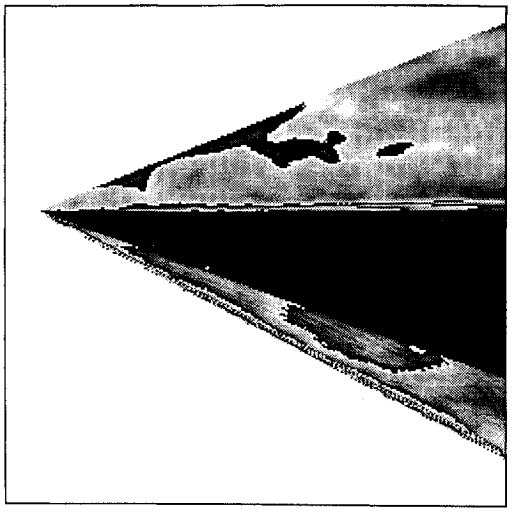

Fig. 17 Phase map obtained by subtraction of the measured phase map of Fig. 13 from the computed phase map of Fig. 15 [interval range $(1/5)\lambda$].

maximum phase difference is observed in the boundary layer and equals $+0.66\lambda$, whereas the minimum phase difference, -0.61λ, is found near the windward shock wave. If the phase maps of Figs. 13, 15, and 17 are related to the average density over the width of the test section, the proportional deviation between the computed and the measured phase map is given by Eq. (2). According to this definition the proportional error over the complete phase map is found to lie in the interval $(-1.8\%, +1.9\%)$, which is of the same order of magnitude as the error interval found for the near 0-deg incidence cone flow. In the following section the error sources, which may explain the observed differences between the experimental data and the numerical data, will be briefly discussed.

IV. Error Analysis

At least four possible error sources can be distinguished: errors in the generation of the experimental test flowfield, errors in the interferometric measurements, errors due to shortcomings of the theoretical model underlying the computational process, and errors in the experimental data serving as input to the numerical process. The four error sources will be discussed in a qualitative way.

A. Nonuniformity of the Supersonic Stream

As was concluded before from Fig. 4, the oncoming supersonic flow has a limited reproducibility between the two exposures of the holographic plate. Besides these unsteady effects the supersonic flow also contains steady deviations from uniform flow conditions that will affect the interferometric measurements.

It is known that the oncoming supersonic stream is not perfectly uniform because the supersonic nozzle has not been corrected for the growth of boundary layers along its contours and along the side walls of the wind tunnel. Furthermore, the oncoming supersonic flow deviates from perfect uniformity due to local surface imperfections of the nozzle and of the wind-tunnel side walls. These surface imperfections give rise to local disturbances of the flow that propagate along Mach lines. Both mentioned steady deviations from uniform supersonic flow conditions are not visible in that part of the phase map of Fig. 4 that corresponds with the undisturbed flow (because they are canceled by taking both exposures of the holographic plate when the wind-tunnel is in operation). However, it will be clear that they will have influenced the phase values measured in the disturbed flow around the cone because of their different impact on the undisturbed flow and on the disturbed flow.

B. Errors in the Interferometric Measurements

The inevitable phase error is likely to be due to a combination of the finite thickness of the emulsion on the holographic plate (7 μm) and the nonuniform photographic processes to which it is subjected. The phase error in the measured phase maps of Figs. 6 and 13 is not due to a random orientation of the holographic plates in the

hologram holder between recording and reconstruction. Errors of this type were shown to be negligible if closely spaced reference beams are used,[8] as is the case in the setup of Fig. 1.

C. Shortcomings of the Theoretical Model

The shortcomings of the theoretical model are twofold. As remarked before, in the computation of the flowfield by the Euler code no boundary layer is modeled at the surface of the cone. Furthermore, in the integration of the three-dimensional density distribution to a phase map, straight ray paths are assumed. This is equivalent to neglecting the refraction of light rays in nonhomogeneous media.

D. Uncertainty in Input Data to Computations

Uncertainties exist in the experimentally determined values of the parameters serving as input to the computational process. Because of the nonuniform flow conditions in the oncoming supersonic flow, the freestream Mach number and the freestream density cannot be assigned unique values. As input to the three-dimensional Euler computation, they were given the values obtained at the location of the pitot pressure probe that was positioned just beneath the area of the test section imaged on the camera as indicated in Fig. 3. Also a small error in the measured angle of incidence of the cone with respect to the main flow direction may yield considerably different results by the Euler computations. In addition, during integration of the three-dimensional density distribution to a two-dimensional phase map, a small error in the determination of the orientation of the cone with respect to the detector grid or in the size of the area in the wind tunnel imaged on the camera may cause differences between the computed phase map and the measured phase map. In particular, this will be the case in those regions of the phase map where strong phase gradients exist. This may explain the larger phase differences found near the shock wave on either side of the cone in Fig. 10 and at the windward side of the cone in Fig. 17.

V. Concluding Remarks

A quantitative comparison has been performed between the experimental data obtained by dual-reference-beam, plane-wave digital holographic interferometry and the numerical data obtained by a three-dimensional Euler code for inviscid flow. The comparison involves the supersonic flow around circular cones for different cone angles and angles of incidence. The agreement between experimental data and numerical data is rather good. The deviations are of the same order of magnitude as the uncertainties in the experimental flow conditions.

Finally, two recommendations with regard to future comparisons are given. It would be more realistic to compare the interferometric data with the numerical data obtained by a computer code based on the Navier–Stokes equations, modeling also viscous effects and boundary layers. Furthermore, a more detailed comparison would be possible if the three-dimensional density distribution in the flowfield is reconstructed by computed tomography from the projection data obtained by repeated application of DHI along different directions through the flowfield.

References

[1]Jones, D. J., "Numerical Solutions of the Flow Field for Conical Bodies in a Supersonic Stream," National Research Council of Canada, Report LR-507, 1968.

[2]Jones, D. J., "Tables of Inviscid Supersonic Flow About Circular Cones at Incidence, $\gamma = 1.4$," Agardograph 137, Pts. I and II, 1969.

[3]Jones, D. J., "Tables of Inviscid Supersonic Flow About Circular Cones at Incidence, $\gamma = 1.4$," Agardograph 137, Pt. III, 1971.

[4]Jagota, R. C., and Collins, D. J., "Finite Fringe Holographic Interferometry Applied to a Right Circular Cone at Angle of Attack," *Journal of Applied Mechanics*, Vol. 39, 1972, pp. 897–903.

[5]Zien, T.-F., Ragsdale, W. C., and Spring, W. C., III, "Quantitative Determination of Three-Dimensional Density Field by Holographic Interferometry," *AIAA Journal*, Vol. 13, 1975, pp. 841, 842.

[6]Lanen, T. A. W. M., Bryanston-Cross, P. J., and Bakker, P. G., "Digital Holographic Interferometry in High-Speed Flow Research," *Experiments in Fluids*, Vol. 13, 1992, pp. 56–62.

[7]Vest, C. M., *Holographic Interferometry*, Wiley, New York, 1979.

[8]Dändliker, R., Thalmann, R., and Willemin, J. F., "Fringe Interpolation by Two-Reference Beam Holographic Interferometry: Reducing Sensitivity to Hologram Misalignment," *Optics Communications*, Vol. 42, 1982, pp. 301–306.